HHS Public Access

Author manuscript

Int J Pharm. Author manuscript; available in PMC 2022 December 14.

Published in final edited form as:

Int J Pharm. 2022 September 25; 625: 122072. doi:10.1016/j.ijpharm.2022.122072.

Tumoral oxygenation and biodistribution of Lonidamine oxygen microbubbles following localized ultrasound-triggered delivery

Quezia Lacerda[a,b], **Ankit Rochani**[c,f], **Brian Oeffinger**[b], **Ji-Bin Liu**[a], **Corinne E. Wessner**[a,b], **Aylin Tahmasebi**[a], **Hebah Falatah**[a,b], **Philip Lee**[a], **Dennis B. Leeper**[d], **Flemming Forsberg**[a], **Joseph Curry**[a], **Scott W. Keith**[e], **Patrick O'Kane**[a], **Gagan Kaushal**[c], **Margaret A. Wheatley**[b], **John R. Eisenbrey**[a,*]

[a]Department of Radiology, Thomas Jefferson University, Philadelphia, PA 19107, USA

[b]School of Biomedical Engineering, Science and Heath Systems, Drexel University, Philadelphia, PA 19104, USA

[c]Department of Pharmaceutical Sciences, Thomas Jefferson University, Philadelphia, PA 19107, USA

[d]Department of Radiation Oncology, Thomas Jefferson University, Philadelphia, PA 19107, USA

[e]Division of Biostatistics, Department of Pharmacology and Experimental Therapeutics, Thomas Jefferson University, Philadelphia, PA 19107, USA

[f]Wegmans School of Pharmacy, Department of Pharmaceutical Sciences, St. John Fisher University, Rochester, NY 14618, USA

Abstract

[*]Corresponding author at: Thomas Jefferson University, 132 South 10th St, Philadelphia, PA 19107, USA., john.eisenbrey@jefferson.edu (J.R. Eisenbrey).

Declaration of Competing Interest

The authors declare that they have no known competing financial interests or personal relationships that could have appeared to influence the work reported in this paper.

CRediT authorship contribution statement

Quezia Lacerda: Data curation, Formal analysis, Funding acquisition, Investigation, Methodology, Resources, Validation, Visualization, Writing – original draft, Writing – review & editing. **Ankit Rochani:** Formal analysis, Investigation, Methodology, Resources, Supervision, Validation, Visualization, Writing – review & editing. **Brian Oeffinger:** Formal analysis, Investigation, Methodology, Resources, Validation, Visualization, Writing – review & editing. **Ji-Bin Liu:** Conceptualization, Formal analysis, Investigation, Methodology, Resources, Supervision, Validation, Visualization, Writing – review & editing. **Corinne E. Wessner:** Formal analysis, Investigation, Methodology, Resources, Validation, Visualization, Writing – review & editing. **Aylin Tahmasebi:** Formal analysis, Investigation, Methodology, Resources, Visualization, Writing – review & editing. **Hebah Falatah:** Formal analysis, Investigation, Methodology, Resources, Visualization, Writing – review & editing. **Philip Lee:** Formal analysis, Investigation, Methodology, Resources, Visualization, Writing – review & editing. **Dennis B. Leeper:** Conceptualization, Investigation, Methodology, Resources, Supervision, Validation, Visualization, Writing – review & editing. **Flemming Forsberg:** Conceptualization, Formal analysis, Investigation, Methodology, Resources, Supervision, Validation, Visualization, Writing – review & editing. **Joseph Curry:** Conceptualization, Formal analysis, Investigation, Methodology, Resources, Validation, Visualization, Writing – review & editing. **Scott W. Keith:** Conceptualization, Formal analysis, Investigation, Methodology, Resources, Visualization, Writing – review & editing. **Patrick O'Kane:** Conceptualization, Investigation, Methodology, Resources, Validation, Visualization, Writing – review & editing. **Gagan Kaushal:** Data curation, Formal analysis, Investigation, Methodology, Project administration, Resources, Supervision, Validation, Visualization, Writing – review & editing. **Margaret A. Wheatley:** Conceptualization, Data curation, Formal analysis, Funding acquisition, Investigation, Methodology, Project administration, Resources, Supervision, Validation, Visualization, Writing – review & editing. **John R. Eisenbrey:** Conceptualization, Data curation, Formal analysis, Funding acquisition, Investigation, Methodology, Project administration, Resources, Supervision, Validation, Visualization, Writing – review & editing.

Prior work has shown that microbubble-assisted delivery of oxygen improves tumor oxygenation and radiosensitivity, albeit over a limited duration. Lonidamine (LND) has been investigated because of its ability to stimulate glycolysis, lactate production, inhibit mitochondrial respiration, and inhibit oxygen consumption rates in tumors but suffers from poor bioavailability. The goal of this work was to characterize LND-loaded oxygen microbubbles and assess their ability to oxygenate a human head and neck squamous cell carcinoma (HNSCC) tumor model, while also assessing LND biodistribution. In tumors treated with surfactant-shelled microbubbles with oxygen core ($SE61O_2$) and ultrasound, pO_2 levels increased to a peak 19.5 ± 9.7 mmHg, 50 s after injection and returning to baseline after 120 s. In comparison, in tumors treated with $SE61O_2$/LND and ultrasound, pO_2 levels showed a peak increase of 29.0 ± 8.3 mmHg, which was achieved 70 s after injection returning to baseline after 300 s ($p < 0.001$). The co-delivery of O_2 and LND via SE61 also showed an improvement of LND biodistribution in both plasma and tumor tissues ($p < 0.001$). In summary, ultrasound-sensitive microbubbles loaded with O_2 and LND provided prolonged oxygenation relative to oxygenated microbubbles alone, as well as provided an ability to locally deliver LND, making them more appropriate for clinical translation.

Keywords

Lonidamine; Microbubbles; Oxygen delivery; Contrast-enhanced ultrasound; Hypoxia; Drug delivery; Head and neck cancer

1. Introduction

Head and neck squamous cell carcinoma (HNSCC) is the sixth most common cancer worldwide. In 2019, there were 65,410 new cases of HNSCC, which accounted for 3.7 % of new cancers and 10,860 HNSCC-related deaths (Siegel et al., 2019; Bray et al., 2018). Tobacco and alcohol consumption contributes to the majority of HNSCC globally, especially tumors within the oral cavity, hypopharynx and larynx (Vigneswaran and Williams, 2014; Marur and Forastiere, 2016). The human papilloma virus contributes to the majority of oropharyngeal tumors in the United States, recently surpassing cervical cancer as the most common HPV-related malignancy and has been called a cancer epidemic (Lechner et al., 2022).

Patients suffering from HNSCC are generally treated with surgical resection or radiation therapy with or without systemic therapy (chemotherapy or immunotherapy) as a primary modality. Radiation is also used frequently in the adjuvant setting. The conventional clinical radiation dose for HNSCC being 1.5–2 Gy per fraction given 5 days/week for up to 7 weeks. Typically, these fractions are delivered over 4–5 min (Halperin et al., 2013). Radiation directly damages the DNA by ionization of atoms, leading to double-stranded DNA breaks (Lehnert, 2007). In addition, radiation therapy creates reactive oxygen species (ROS), which in turn can cause irreversible DNA damage in tumor cells (Srinivas et al., 2019). Ultimately, both mechanisms result in chromosome aberrations, apoptosis and necrosis of cancer cells and destruction of tumor vessels. However, tumors are often more resistant than the surrounding normal tissue to radiation effects.

Chronic hypoxia and consequent limited production of ROS has been identified as the key mechanism of radiation therapy resistance in tumors (Brown and Wilson, 2004; Rockwell et al., 2009). The aberrant vasculature that forms in the tumor by angiogenesis cannot supply sufficient oxygen to the cells: It is estimated that 10–30 % of solid tumor mass is made up of hypoxic and/or anoxic areas (oxygen partial pressure (pO_2) of 0–20 mmHg) heterogeneously distributed within the tumor (Brown and Wilson, 2004; Moulder and Rockwell, 1984). As these hypoxic regions are relatively insensitive to chemotherapy and radiation therapy, they facilitate tumor progression, leading to poor clinical outcomes (Knowles and Harris, 2001). In HNSCC tumors, hypoxia during radiotherapy is an independent predictor of patient survival (Nordsmark et al., 2005). Remarkably, an increase as small as 10 mmHg in pO_2 in hypoxic tissue significantly improves sensitivity to radiation therapy. The increase in pO_2 primarily increases sentivity in hypoxic cells, but does not affect the sensitivity of surrounding normally oxygenated tissue (Rockwell et al., 2009). As a result, ultrasound-guided delivery of oxygen has gained special attention in recent years, since it allows spatially confined delivery into target areas while minimizing systemic toxicity (Mullick Chowdhury et al., 2017; Eisenbrey et al., 2015).

Ultrasound-sensitive microbubbles containing oxygen (surfactant-shelled microbubble with oxygen core [$SE61O_2$]) for localized oxygen delivery prior to radiation therapy have been previously proposed and evaluated by our group (Eisenbrey et al., 2015). Studies *in vivo* showed that in animals receiving $SE61O_2$ followed by ultrasound and radiation, the intratumoral pO_2 was elevated by 19.7 ± 9.1 mmHg, which improved the efficacy of radiation therapy dramatically, resulting in decreased tumor growth and increased survival (Eisenbrey et al., 2018). However, the duration of oxygenation using this platform was limited (2–3 min), making clinical translation difficult (oxygenation is required for at least 4–5 min in most clinical applications) (Halperin et al., 2013). In the current study, we investigated ways to overcome the limitations of our groups' current O_2 microbubble platform by combining localized delivery of O_2 with a pharmacologic respiration inhibitor, thereby extending the duration of oxygenation for better clinical outcomes.

The therapeutic agent lonidamine (LND) targets glycolysis and mitochondrial respiration in tumors (Nancolas et al., 2016). LND also shows selectivity against a broad range of tumors with little effect on normal tissues at levels below 400 mg/m^2 (oral or IV dosing) as well as a lack of combined side effects when administered with other chemotherapeutic drugs (Nath et al., 2016; Huang et al., 2020). LND has been shown to depress the energy metabolism of tumor cells, causing mitochondrial damage and an inhibition of oxygen consumption (Magno et al., 1994; Nath et al., 2016). However, clinical translation has stalled due to poor bioavailability after oral administration and showed severe side effects when LND was administered intravenously, presumably due to the molecule's hydrophobicity (Price et al., 1996). By encapsulating LND within the hydrophobic portion of the surfactant shell of $SE61O_2$, we attempted to circumvent its solubility issues with the hopes that treatment could be augmented by co-delivering LND along with oxygen. The purpose of this study was to extend our previous oxygen delivery findings in a breast cancer model to an HNSCC tumor model, and to assess the potential of encapsulated LND. We hypothesized that the addition of LND will lower the rate of consumption of O_2, thus prolonging the elevated pO_2 levels in the tumor, enabling sufficient time for external beam radiotherapy in future

work. Additionally, ultrasound-guided delivery of LND may overcome or mitigate existing bioavailability issues.

2. Materials and methods

2.1. Microbubble fabrication

Surfactant-shelled oxygen microbubbles loaded with LND (Sigma-Aldrich; St. Louis, MO) were fabricated by modifying our previously reported methods (Eisenbrey et al., 2015, Oeffinger et al., 2019; Vaidya et al., 2021). The LND was first entrapped in water-soluble vitamin E, Tocopheryl polyethylene glycol succinate (TPGS) (Eastman Chemical Company; Kingsport, TN) micelles, by incubating the mixture while stirring for 48 hrs at 37 °C. The micelle mixture was then mixed with autoclaved sorbitan monostearate (SEPPIC Inc./Air Liquide, Fairfield, NJ) solution and allowed to cool overnight. All subsequent steps remained the same as in our reported methods for unloaded microbubbles (Vaidya et al., 2021). Solutions were first purged with perfluorocarbon (PFC) gas (Octafluoropropane, Advanced Specialty Gasses; Reno, NV) followed by sonication in the presence of the PFC and the resultant microbubbles were separated using gravity to create surfactant-shelled microbubbles (SE61) in solution. The resulting microbubble solution was diluted 1:1 (v/v) with 10 % (w/v) glucose acting as a lyoprotectant, with 2 mL aliquots placed into 10 mL vials. Samples were frozen in a −20 °C bath and then freeze-dried under vacuum for at least 20 hrs and capped under vacuum. For reconstitution before use, microbubbles were charged with sterile-filtered (0.2 μm filter) gas of choice, PFC or oxygen (Airgas, Radnor, PA) through the vial stoppers using a syringe needle and reconstituted immediately before use by injecting 2 mL of 0.5 × phosphate buffered saline (PBS).

2.2. In vitro acoustic characterization

Acoustic enhancement and stability were quantified *in vitro* following a previously published protocol using a custom-built 50 mL acrylic acoustic sample holder submerged in a 37 L tank filled with DI water at 37 °C (Eisenbrey et al., 2015). This was tested using a 5 MHz single element transduce focused trough the acoustic window of the sample holder, which generated a peak positive pressure of 0.69 MPa and a peak negative pressure (PNP) of 0.25 MPa at a PRF of 100 Hz. All reconstituted samples were stored at room temperature, approximately 22 °C, until use. Non-cumulative dose–response curves for all microbubble samples were constructed by pipetting increments of reconstituted bubbles into the sample holder containing 50 mL with continually stirred warm PBS (37 °C). Microbubbles were allowed to mix for 10 s to ensure a homogenous media before measuring the acoustic response. To examine the stability of all samples a dose along the rise of the dose–response curve (280 μL/L) was insonated continuously over a 10 min period using the same acoustic parameters employed for the dose–response. Readings were taken every minute, starting at t = 0 for a total of 11 readings. The data were normalized to the initial reading (i.e., at t = 0).

2.3. Microbubble Lonidamine loading quantification

The amounts of LND in the samples were quantified using the Dionex Ultimate 3000 HLPC system (ThermoFisher, Waltham, MA) attached with Thermo Orbitrap mass spectrometer. Chromatographic separations were carried out using XBridge C18 column (4.6 mm × 150

mm, 3.5 μm; Waters). Two mL of methanol was added to each of the freeze-dried sample vials and vortexed for 15–20 s. One mL of the sample was transferred to an HPLC vial using a syringe filter. The mobile phase was composed of 50 % solvent A (0.1 % formic acid in water) and 50 % solvent B (0.1 % formic acid in acetonitrile) (Rochani et al., 2020). The mobile phase was chosen to be acidic to promote complete ionization of LND, at a flow rate of 0.2 mL/min. For all studies, the temperature of the sample compartment was maintained at 4 °C and the column temperature at 30 °C. The injection volume was 5 μL with a run time of 17 min. Our drug of interest, LND is a positively charged weak base with a positive polarity. A transition of 305/322 *m*/*z* was used for the LND detection in the MS. The sheath gas flow rate was 30 PSI and capillary temperature 350 °C and the capillary voltage was 52.40 V. In preliminary studies, each peak depicted 100 % relative abundance corresponding to the known molecular weight of LND (321.02) and retention time of 15 min.

2.4. SE61 microbubble size and counts

Microbubbles were counted and sized using a PSS AccuSizer FX Nano (Entegris, Port Richey) which uses the technique of single particle optical sizing, resulting in a number-based population count. Reconstituted microbubble samples were diluted by a factor of 100 in a 1:99 (v/v) ratio, by adding 10 μL of reconstituted microbubble to 990 μL of deionized water (DI) (ACS reagent, ASTM Type I). From the dilution of microbubble and DI water, 20 μL were injected into an automatic dilution chamber containing filtered DI water. Measurements were done using an LE sensor with a range of 0.5 to 200 μm.

2.5. Lonidamine plasma and tissue distribution determination

2.5.1. Sample preparation for plasma and tissue biodistribution—

All the test and standard spiked plasma and tissue samples were extracted using a protein precipitation method with acetonitrile (ACN), where plasma to ACN ratio (v/v) was 1:3 and 1-benzyl imidazolyl-3-carboxylic acid (1 μg/mL) was used as an internal standard. Extraction of drug from the tissue was adopted from a previously published study (Milane et al., 2011). Tissues were homogenized using a mechanical homogenizer (850 Homogenizer; Fisher Scientific; Waltham, MA) in 1 mL buffer (10 mM Tris, 1 mM EDTA, and 10 % (v/v) glycerol (pH 7.4)). Later, LND was extracted in ACN 1:3 ratio (v/v) with tissue homogenate. Extracted plasma standards, test plasma, and tissue samples were vortexed and later centrifuged for 10 min at 16,392 g force with rotor radius of 84 mm. The clear supernatant was then subjected to LCMS analysis.

2.5.2. Plasma and tissue LND quantification method—

A liquid chromatography mass spectrometry (LCMS) method used for quantification of LND from plasma and tissues was adopted from our previously reported publication (Rochani et al., 2020). A Dionex 3000 UHPLC system was used for performing chromatographic separation of LND. Drug was separated on Xbridge C18 (4.6 × 75 mm, 2.5 μm) reverse phase column (Waters Corporation, Milford, MA) using isocratic elution method with 50:50 (water 0.1 %FA: ACN 0.1 %FA), at 0.25 mL/min flow rate. The temperature of the column was maintained at 30 °C with constant data acquisition for 20 min of run time. The injection volume was set to 10 μL. Detection of LND was performed using a Thermo Exactive mass spectrometer (MS) (Waltham, MA) under positive ion mode. For detection, ionization voltage 4.5 kV, sheath

gas flow rate 30, auxiliary gas flow rate 5, and capillary temperature 375 °C were used. Mass spec tune file was generated by automatic tune function of Xcalibur software to get optimum capillary voltage, tube lens voltage, skimmer voltage to get *m*/*z* single for target ion of $(M + H)^+$ 321.02 *m*/*z* with the intensity of ~ 10^7 for the standard drug in ACN 0.1 %FA. Scanning mass range for the MS method was set at 100 to 325 *m*/*z*. Exactive (v 1.1SP6) software was used for MS method development and data acquisition. Thermo Excalibur (v 3.0.63) was used for sample injections and LC-MS data acquisition.

2.6. Cell line and reagents

The human HNSCC cell line CAL27 was purchased from ATCC (Manassas, VA). Cells were maintained in Dulbecco's modified Eagle's medium (DMEM), High Glucose, Gluta MAX™ (Gibco™, Waltham, MA) supplemented with 10 % fetal bovine serum (Corning, NY) and 1 % penicillin–streptomycin (ATCC, Manassas, VA). Cell lines were cultured in a humidified 37 °C incubator with 5 % carbon dioxide. Experiments were performed with cells from passage 3–10.

2.7. Implantation and tumor growth

Human HNSCC tumors were generated in 56 immunodeficient, nude mice (The Jackson Lab, Bar Harbor, ME) (split evenly by gender) by injecting 5×10^5 CAL27 cells (ATCC, Manassas, VA) mixed with 100 μL matrigel (Corning, NY) subcutaneously on the right flank. The animal protocol was approved by Thomas Jefferson University's Institutional Animal Care and Use Committee. Tumors were grown to approximately 100 mm^3 before animals were randomly assigned to treatment groups. This size was selected to provide tumors with an active blood supply, while still being large enough to accommodate a pO_2 probe (OxyLite 2000 system) for oxygen monitoring. Tumor-bearing animals were assigned to the treatment groups listed in Table 1.

2.8. Treatment administration

Animals in the LND pretreatment group without $SE61O_2$, received an intraperitoneal injection of LND (IP LND) equivalent to the amount of LND encapsulated in $SE61O_2$/LND (~25 μg/mL) suspended in tris/glycine buffer 45 mins prior to serum collection and photoacoustic imaging based on previous radiosensitization work (Kim et al., 1984, 1986; Nath et al., 2016). Animals in the SE61 groups received microbubble administrations in randomized order through a 24-gauge tail vein angiocatheter. Each SE61 group had 0.1 mL bolus injection of agent followed by a 0.05 mL saline flush during ultrasound triggering at the tumor and 0.1 mL bolus of agent without ultrasound triggering followed by a 0.05 mL saline flush. Continuous imaging in B-mode and contrast mode was acquired using a 10L4 transducer and aAcuson Sequoia (Siemens Healthineers, Mount View, CA). At peak enhancement, a destructive pulse was employed to destroy microbubbles within the tumor (MI = 1.4) followed by 10 s of low mechanical index (MI) imaging to visualize reperfusion (MI = 0.12). This process was repeated for the duration of contrast enhancement (3–5 min).

2.8.1. Plasma sampling and preparation—For serum analysis, 10 μL of 10 % ethylenediamine tetraacetic acid (EDTA) solution was added to each 1.5 mL Eppendorf tube prior to collection. Fifty μL of blood was collected from the venous sinus at baseline,

15 mins post injection, and at time of sacrifice (2, 24, 72 hrs.) and tubes were stored on ice. Samples were then centrifuged at 16,392 g force for 10 mins to separate the plasma from whole blood. The plasma was then collected and stored in a −80 °C freezer. The extraction of drug from the plasma was adopted from a previously published work (Milane et al., 2011), where LND was extracted in 1:3 v/v ratio for plasma and ACN. Extracted plasma standards were vortexed and centrifuged 10 min at 16,392 g force, and subjected to LCMS analysis.

2.8.2. Tissue collection and processing—At each time of sacrifice (2, 24, and 72 hrs) organs harvested (heart, kidney, liver, lung, spleen, and tumor) were weighed and homogenized in a 10:1 (v/w) ratio of buffer (10 mM Tris, 1 mM EDTA, and 10 % (v/v) glycerol (pH 7.4)). Tissue samples were then prepared as described above where LND was extracted in 1:3 ratio of tissue homogenate to ACN. All samples were vortexed and later centrifuged 10 min at 16,392 g force. The clear supernatant was then subjected to LCMS analysis.

2.9. Oxygen delivery experiments

Oxygen delivery experiments were modeled after our previous published findings (Eisenbrey et al., 2018) where the intratumoral oxygen kinetics were measured using an OxyLite 2000 bare fiber probe (Oxford Optronix, Oxford, United Kingdom). Additionally, photoacoustic imaging was performed pre- and post-treatment using a Vevo 2100 LAZR system (Fujifilm VisualSonics, Toronto, Canada) with a 24 MHz probe to assess changes in hemoglobin oxygenation. The extent and duration of changes to intratumoral pO_2 were first quantified using the OxyLite system, which directly measures the pO_2 levels using fiberoptics (Griffiths and Robinson, 1999). Half of the animals from each group listed in Table 1 with tumors grown to 5–8 mm diameter were anesthetized using a mixture of ketamine (75 mg/kg subcutaneously) and acepromazine (1 mg/kg subcutaneously) and placed on a warming blanket. Prior to microbubble or control injection, a 24-gauge catheter was placed into the tumor interstitium under ultrasound guidance. A fiberoptics pO_2 probe connected to an OxyLite 2000 system was introduced through the catheter and the tip location was visually confirmed by the fluorescent light at the tip of the probe. Following placement, both the probe and animal were taped to the warming blanket to minimize movement during scanning. Baseline pO_2 levels were recorded. Microbubble injections were performed through a 24-gauge tail-vein catheter. All animals received a 0.1 mL bolus of SE61 with and without LND, with either O_2 or PFC gas, followed by a 0.05 mL saline solution flush. Following administration, the flash-replenishment sequence was repeated for the duration of microbubble detection. Real-time pO_2 levels were recorded every 10 s during injection. This process was repeated until pO_2 levels returned to baseline levels and no microbubbles were visible on ultrasound. All of the animals underwent photoacoustic imaging experiments on a Vevo2100 LAZR system with an LZ250 probe. Tumor-bearing animals were prepared as described above. Changes in intratumoral oxygenation percentage were quantified by subtracting the 3D average pre-treatment oxygen saturation (sO_2) value from post-treatment. These values were obtained by drawing ROIs of tumors for each animal pre-and post-treatment administration. The values for each animal were organized according to the groups. A one-way Anova test was run between the groups.

2.9.1. Data analysis—Tumoral oxygenation measured using the OxyLite system was plotted as a function of time for each group. For photoacoustic imaging experiments, each animal that was scanned had region of interest drawn across the tumor image using the VevoLabs software (VisualSonics) where the changes in tissue and tumor hemoglobin oxygenation levels after treatment were calculated. One way ANOVA test was run between the animals in each groups using GraphPad Prism version 9.0.2 (161) for Windows (GraphPad Software, San Diego, CA USA). For biodistribution of LND, generalized linear models (Liang & Zeger, 1986) using generalized estimating equations (GEE) (Hardin and Hilbe, 2002) and a compound symmetric working correlation structure for robust error variance estimation were constructed to estimate the effects of treatment on log(LND + 1) over log(hours) and between different tissues. Separate linear models were constructed for the subgroup of tumor site observations. Separate longitudinal generalized linear models with autoregressive working correlation structures were constructed to estimate the effects of treatment on log (LND + 1) over log (hours) in plasma. Selections between the 2-way interaction and main effects-only models were made using quasilikelihood information criterion. The significance level for each hypothesis test was set at a nominal $\alpha = 0.05$.

3. Results

3.1. SE61O_2 microbubble size and counts

Microbubble yields and diameters were calculated from data acquired above 0.8 μm since measurements below 0.8 μm were considered to be residual surfactant particles. This was based on the observation that samples taken from vials in which the bubbles had been allowed to decay had demonstrated no measurable echogenicity but, nonetheless, produced a matching size distribution below 0.8 μm. Drug or gas did not have a significant effect on microbubble size population. The weight mean diameter between range 0.80 – 19.74 μm as a function of D10, D50 and D90 was 0.32, 0.55 and 1.89 μm respectively. Average size and concentration for SE61O_2, SE61O_2/LND and SE61$_{PFC}$, were 1.65 μm, $p = 0.86$ and mean bubble concentration $(1.6 \pm 0.2) \times 10^9$, $(2.7 \pm 0.2) \times 10^9$ and $(1.8 \pm 0.4) \times 10^9$ respectively; $p = 0.12$.

3.2. In vitro acoustic characterization

Acoustic enhancement and stability were quantified in the *in vitro* tank. Non-cumulative dose–response curves for SE61O_2, SE61O_2/LND and SE61$_{PFC}$ were constructed by pipetting increments of each sample into the sample holder containing 50 mL of continually stirred warm PBS (37 °C). No statistically significant changes in maximum acoustic enhancement were observed for SE61O_2, SE61O_2/LND or SE61$_{PFC}$, 18.09 ± 0.86 dB, 17.61 ± 1.2 dB and 17.89 ± 0.56 dB respectively; $p = 0.87$) as shown in Fig. 1. Similarly, to examine the *in vitro* stability of each sample a dose of 280 μL/L was insonated continuously over a 10 min period using the same acoustic parameters as outlines for the dose–response. Readings were taken every minute, starting at $t = 0$ for a total of 11 readings. The data were normalized to the initial reading at $t = 0$. Stability curves showed an acoustic half-life between 1.5 and 2.2 min for all SE61 samples ($p = 0.73$; Fig. 2).

3.3. Microbubble Lonidamine loading quantification

Microbubbles loaded with LND ($SE61O_2$/LND) had an average encapsulation of 25.7 ± 1.5 μg/mL, surpassing the minimum required drug loading of least 4.8 μg/mL assuming 20 % delivery (Patel et al.2022). This metric is based on an anticipated tumor volume of 100 mm^3, where Floridi et al. (1981) calculated that a minimum effective lonidamine dose in tissue culture was 3 μM. The maximum injectable dose in mice is 0.1 mL.

3.4. Microbubble imaging in vivo and initial tolerability

All microbubbles whether oxygenated, charged with PFC and/or drug loaded ($SE61O_2$, $SE61O_2$/LND and $SE61_{PFC}$) were well-tolerated following intravenous injection. All agents also perfused well into the tumor environment with marked enhancement on the ultrasound scanner (Fig. 3). Following administration, agents circulating through the ultrasound beam were noninvasively destroyed with a flash-replenishment sequence that was repeated for the duration of microbubble detection (3–5 min), confirming the ability to not only destroy these agents locally but also confirming their stability in the systemic circulation. An example of this is shown in Fig. 3, where the left size of the display are the nonlinear imaging mode (contrast) and the right the conventional B-mode (grayscale imaging). Images were taken prior to $SE61O_2$/LND injection, beginning of microbubble perfusion into the tumor, complete perfusion of the tumor environment, during the destruction of the microbubbles at higher MI pulses, and when the microbubbles reperfused into the tumor environment after the destructive pulse.

3.5. Calibration of Lonidamine concentrations over time

Representative LCMS spectra for LND and internal standard are provided in Fig. 4 (a and b). Due to structural similarities, 1-benzyl imidazolyl-3-carboxylic acid was used as an internal standard (ISD) for the development of LCMS plasma assay. Retention times of LND and ISD were found to be 17.07 min ± 0.50 min. and 7.79 ± 0.50 min, respectively. A linear curve was established for LND in the range of 15 to 2000 ng/mL in plasma for two sets injected on four different days accounting for n = 8 (2×4) injections. The inter and intraday % accuracy and % coefficient of variance (%CV) for calibration were within 100 ± 10 % and < 10 %, respectively. The linearity equation was found to be $y = 6661.7x$, $r^2 > 0.99$. The lower limit of detection (LOD), and lower limit of quantitation (LOQ) for the quantitation of the assay were 5 ng/mL and 15 ng/mL, respectively. Representative spectra for LND and LOD and LOQ for the assay and corresponding ISD peaks are provide in Fig. 4 (e) and (f). This plasma quantitation and LCMS run was extended later for the quantitation of LND in tissue homogenate to account for tissue distribution of microbubble. Fig. 4 (g) shows a consistent recovery of LND extracted in ACN from all the tissues and the peak was observed around 17 min compared to corresponding blank tissue extracts.

3.5.1. Lonidamine plasma biodistribution over time—

The plasma concentration of LND was analyzed over the time course of 0 to 72 hrs (0–24 hrs shown in Fig. 5). Groups that received $SE61O_2$ loaded with LND and ultrasound demonstrated serum concentrations of 1074 ± 440 ng/mL at 15 min post injection while animals that received $SE61O_2$ with LND and no ultrasound triggering demonstrated serum concentrations of 528 ± 127 in

both groups (no LND detected at 72 hrs.). Even without ultrasound triggering, the bubbles will eventually degenerate and release the LND entrapped on its shell as shown in Fig. 5. Animals placed in the pretreatment group of LND that received an IP injection of LND had a serum concentration of 3184 ± 787 ng/mL of LND at 45 min. LND concentrations in plasma after IP LND treatment tended to be significantly higher than after SE61O_2/LND with ultrasound triggering ($p < 0.001$), but LND concentrations in plasma were similar between SE61O_2/LND with and without ultrasound ($p = 0.29$). As expected, there was no concentration of LND found in plasma for groups treated with SE61 charged with either PFC or O_2 (without LND) regardless of ultrasound triggering.

3.5.2. Lonidamine tissue biodistribution over time—The LND concentration over time (2–72hrs) in tissue is shown in Fig. 6. Independent of time since treatment or tissue site, LND concentrations after SE61O_2/LND with ultrasound triggering was significantly higher than after SE61O_2/LND without ultrasound triggering ($p = 0.014$), but not statistically significantly higher than after IP LND treatment ($p = 0.28$). Importantly, LND concentrations in tumor tissue after SE61O_2/LND with ultrasound triggering was significantly higher than after SE61O_2/LND without ultrasound triggering ($p < 0.001$), where the LND concentration in tumors harvested at 2 hrs. reached 1194 ± 435 ng of LND/g of tumor compared to the non-ultrasound triggering group 22.6 ± 12.2 ng of LND/g of tumor ($p = 0.002$) but not significantly higher than after IP LND treatment ($p = 0.88$). As no treatment-by-log (hours) interaction was detected, results of a linear model of log (LND + 1) with terms of treatment and log (hours) are presented in Table 2.

3.6. Monitoring of intratumoral pO_2

OxyLite measurements showing the average intratumoral pO_2 are shown in Fig. 7. No changes in pO_2 levels were detected after IP injection of LND, SE61$_{PFC}$, SE61O_2 and SE61O_2/LND without ultrasound exposure. In tumors treated with SE61O_2 and ultrasound, pO_2 levels increased in all animals to a peak of 19.5 ± 10 mmHg with peak oxygenation achieved 50 s after injection and returning to baseline after 120 s. In comparison, pO_2 levels in animals treated with SE61O_2/LND and ultrasound achieved a peak increase of 29.1 ± 8.3 mmHg with peak oxygenation achieved 70 s after injection and returning to baseline after 300 s ($p < 0.001$). However, photoacoustic imaging showed no changes in hemoglobin oxygenation across treatment groups ($p = 0.18$; example shown in Fig. 8).

4. Discussion

Ultrasound-sensitive microbubbles are playing an emerging role within radiation oncology (Lacerda et al.2021). Ultrasound triggered microbubble destruction (without O_2) has been explored as a therapeutic tool to increase endothelial cell radiosensitivity by inducing cell apoptosis due to the increased ceramide production from the shear stress caused by inertially cavitating microbubbles (Kolesnick and Fuks, 2003; Czarnota, 2015; Daecher et al., 2017; El Kaffas et al., 2018). These mechanisms have also recently been shown to improve radiosensitivity to transarterial radioembolization in an ongoing clinical trial (Eisenbrey et al., 2021). Additionally, the ability to locally deliver a payload of choice via ultrasound guided microbubble destruction has shown promise for localized O_2 delivery. This has been

explored both *in vivo* and *in vitro* (Cochran et al., 2011; Kheir et al., 2012; McEwan et al., 2015; Fix et al., 2018; Reusser et al., 2020).

Our group demonstrated that oxygen microbubbles ($SE61O_2$) triggered with ultrasound can locally elevate oxygen levels in mice with breast tumor xenografts (Eisenbrey et al., 2015, 2018) showing that animals treated with $SE61O_2$ triggered with ultrasound demonstrated a peak increase of 19.7 ± 9.1 mmHg. These results demonstrate the feasibility of using $SE61O_2$ to locally deliver enough O_2 to hypoxic tumors to improve radiotherapy outcomes. However, the duration of oxygenation was somewhat short-lived (<2 mins), suggesting the need for approaches that would increase duration of oxygenation.

In HNSCC tumors, hypoxia is an independent predictor of patient survival. For this reason, we investigated the ability of a microbubble platform to co-deliver both oxygen and a pharmacologic tumor respiration inhibitor, LND, to HNSCC tumors in order to prevent the cell from compensating for the loss of glycolytic ATP and up-regulating oxidative phosphorylation, which would extend the duration of oxygenation. Previous toxicity work has shown that this surfactant platform is safe and easily customizable (Forsberg et al., 2010). The work reported in this paper supports the safety profile of our microbubble platform, showing great tolerability and penetration into the tumor environment with rapid destruction and reperfusion as demonstrated in Fig. 3. We also found that the acoustic properties of the microbubble platform did not show any significant differences ($p = 0.76$) *in vitro* regardless of drug content and gas $SE61O_2$, $SE61O_2$/LND and $SE61_{PFC}$.

In our previous study (Eisenbrey et al., 2018), $SE61O_2$ triggered with ultrasound provided an intratumoral pO_2 level increase in all animals of 19.46 ± 9.7 mmHg. In the current study, the co-delivery O_2 and LND via ultrasound-sensitive microbubbles ($SE61O_2$/LND) achieved a peak increase of 29.05 ± 8.3 mmHg, and prolonged oxygenation relative to oxygenated microbubbles alone ($p < 0.001$), with levels remaining elevated for up to 5 min. These results are highly encouraging, because they demonstrate that the microbubble platform was able to deliver significant amounts of O_2 intratumorally and that LND was able to extend the duration of elevated O_2 levels within these tumors. However, a limitation in the oxygenation experiments is that the single point measurement in the tumor done with the OxyLite probe averages over an area larger than the microelectrode, which limits the ability to assess for heterogeneity in the pO_2 distribution, as shown by Braun et al. (2001). Photoacoustic imaging has the potential to provide a more global quantification of changes in tumor oxygenation. However, in this study no statistically significant changes in photoacoustic-based oxygenation were observed during treatment. These findings are consistent with our prior studies and are attributed to the fact that photoacoustic oxygenation measurements rely on hemoglobin binding with the O_2 molecule, whereas the delivery of O_2 with the SE61 platform has been shown to be independent of hemoglobin transport (Eisenbrey et al., 2018).

The co-delivery of O_2 and LND via ultrasound-sensitive microbubbles showed an improvement of LND biodistribution in both plasma and tumor tissues. Independent of time since treatment or tissue site, LND concentrations after $SE61O_2$/LND with ultrasound triggering were significantly higher than after $SE61O_2$/LND without ultrasound triggering

($p = 0.014$) illustrating the platform's ability to locally deliver LND. While IP injection of LND showed higher levels of drug in both plasma and tissue, this approach lacked tumor specificity at any time point. It is also not practical to serially administer IP injections in humans (for example in this application 5 times a week for up to 7 weeks).

Several limitations exists in this study. Results reported in this study come from experiments done in athymic nude mice with lack of evidence of how this platform would be able to oxygenate tumors in a syngeneic mouse HNSCC tumor model as well as not showing any therapeutic benefit at this point. The biodistribution time intervals proved to be insufficient to evaluate the PK profiles but were enough to satisfy our main objective of checking the concentration over time in the *in vivo* system to achieve a basic understanding of LND release from the bubbles and clearance (after it was injected) under the influence of ultrasound. Additionally, 8 out of 200 plasma samples were outside the range of 15 to 2000 ng/mL in the linear curve for LND. The high concentration samples were diluted to make sure that they fell within the standard curve range and then adjusted for the concentration with the dilution factor. Future work will be done to evaluate this platform's ability to overcome HNSCC hypoxia induced radio-resistance in human cell line xenografts in both nude mice and syngeneic model.

The therapeutic efficacy of delivering oxygen via SE61 prior to radiation therapy was previously explored by our group in a murine breast tumor model with encouraging results. That study found that an experimental group receiving $SE61O_2$ with ultrasound triggering followed by radiation showed improved tumor control, with a tumor growth delay of approximately 25–35 days and a significantly lower growth rate than all other control groups (Eisenbrey et al.2018). The $SE61O_2$ platform was also shown to enhance tumor response to radiotherapy in a murine model of metastatic breast cancer in the brain (Delaney et al.2019), further suggesting that the local delivery of oxygen can sensitize tumors to radiation. Based on the findings reported in this paper, we plan to explore whether the ultrasound-triggered $SE61O_2$ platform in combination with LND will significantly improve both tumor control and survival in a HNSCC tumor model.

5. Conclusions

This work showed that the co-delivery of O_2 and LND via ultrasound-sensitive microbubbles provided sustained oxygenation relative to oxygenated microbubbles alone and improved LND biodistribution in both plasma and tumor tissue. This supports the platform's ability to locally deliver LND, making it more useful for clinical applications, including enhanced sensitization of HNSCC tumors to radiotherapy.

Acknowledgments

Funding for this work was provided in part by the United States National Institute of Health R01 EB026881 and an equipment support from Siemens Healthineers, Mountain View, California. Montane 60 PHA Premium was a generous gift from Seppic (Paris, France).

Data availability

Data will be made available on request.

References

Braun RD, Lanzen JL, Snyder SA, Dewhirst MW, 2001. Comparison of tumor and normal tissue oxygen tension measurements using oxylite or microelectrodes in rodents. Am. J. Physiol.-Heart Circulatory Physiol. 280 (6).

Bray F, Ferlay J, Soerjomataram I, Siegel R, Torre L, Jemal A, 2018. Global cancer statistics 2018: GLOBOCAN estimates of incidence and mortality worldwide for 36 cancers in 185 countries. CA Cancer J. Clin. 68 (6), 394–424. [PubMed: 30207593]

Brown J, Wilson W, 2004. Exploiting tumour hypoxia in cancer treatment. Nat. Rev. Cancer 4 (6), 437–447. [PubMed: 15170446]

Cochran MC, Eisenbrey JR, Soulen MC, Schultz SM, Ouma RO, White SB, Furth EE, Wheatley MA, 2011. Disposition of ultrasound sensitive polymeric drug carrier in a rat hepatocellular carcinoma model. Acad. Radiol. 18 (11), 1341–1348. [PubMed: 21971256]

Czarnota GJ, 2015. Ultrasound-stimulated microbubble enhancement of radiation response. Biol. Chem. 396, 645–657. [PubMed: 25741736]

Daecher A, Stanczak M, Liu JB, Zhang J, Du S, Forsberg F, Leeper DB, Eisenbrey JR, 2017. Localized microbubble cavitation-based antivascular therapy for improving HCC treatment response to radiotherapy. Cancer Lett. 28 (411), 100–105.

Delaney LJ, Ciraku L, Oeffinger BE, Wessner CE, Liu JB, Li J, Nam K, Forsberg F, Leeper DB, O'Kane P, Wheatley MA, Reginato MJ, Eisenbrey JR, 2019. Breast cancer brain metastasis response to radiation after microbubble oxygen delivery in a murine model. J. Ultrasound Med. 38, 3221–3228. [PubMed: 31124171]

El Kaffas A, Al-Mahrouki A, Hashim A, Law N, Giles A, Czarnota GJ, 2018 Sep 1. Role of acid sphingomyelinase and ceramide in mechano-acoustic enhancement of tumor radiation responses. J. Natl. Cancer Inst. 110 (9), 1009–1018. [PubMed: 29506145]

Eisenbrey J, Albala L, Kramer M, et al. , 2015. Development of an ultrasound sensitive oxygen carrier for oxygen delivery to hypoxic tissue. Int. J. Pharm. 478 (1), 361–367. [PubMed: 25448552]

Eisenbrey JR, Forsberg F, Wessner CE, Delaney LJ, Bradigan K, Gummadi S, Tantawi M, Lyshchik A, O'Kane P, Liu JB, Intenzo C, Civan J, Maley W, Keith SW, Anton K, Tan A, Smolock A, Shamimi-Noori S, Shaw CM, 2021. US-triggered microbubble destruction for augmenting hepatocellular carcinoma response to transarterial radioembolization: a randomized pilot clinical trial. Radiology 298 (2), 450–457. [PubMed: 33320067]

Eisenbrey J, Shraim R, Liu J, et al. , 2018. Sensitization of hypoxic tumors to radiation therapy using ultrasound-sensitive oxygen microbubbles. Int. J. Radiat. Oncol. Biol. Phys. 101 (1), 88–96. [PubMed: 29477294]

Fix SM, Papadopoulou V, Velds H, Kasoji SK, Rivera JN, Borden MA, Chang S, Dayton PA, 2018. Oxygen microbubbles improve radiotherapy tumor control in a rat fibrosarcoma model: a preliminary study. PLoS One 13, e0195667. [PubMed: 29630640]

Floridi A, Paggi MG, Silverstrini B, et al. , 1981. Lonidamine, a selective inhibitor of aerobic glycolysis in murine tumor cells. J. Natl. Cancer Inst. 66, 497–499. [PubMed: 6937706]

Forsberg F, Liu J-B, Patel M, et al. , 2010. Preclinical acute toxicology study of surfactant-stabilized ultrasound contrast agents in adult rats. Int. J. Toxicol. 29 (1), 32–39. [PubMed: 20008819]

Griffiths JR, Robinson SP, 1999. The oxylite: a fibre-optic oxygen sensor. Br. J. Radiol. 72 (859), 627–630. 10.1259/bjr.72.859.10624317. [PubMed: 10624317]

Halperin EC, Brady LB, DE, Perez CA, May 6, 2013. Perez & Brady's Principles and Practice of Radiation Oncology. Lippincott Williams & Wilkins.

Hardin JW, Hilbe JM, 2002. Generalized estimating equations: Hardin James W., Joseph M. Hilbe Taylor & Francis.

Huang Y, Sun G, Sun X, Li F, Zhao L, Zhong R, Peng Y, 2020. The potential of lonidamine in combination with chemotherapy and physical therapy in cancer treatment. Cancers 12 (11), 3332. [PubMed: 33187214]

Kheir JN, Scharp LA, Borden MA, Swanson EJ, Loxley A, Reese JH, Black KJ, Velazquez LA, Thomson LM, Walsh BK, Mullen KE, Graham DA, Lawlor MW, Brugnara C, Bell DC, McGowan

FX Jr., 2012. Oxygen gas-filled microparticles provide intravenous oxygen delivery. Sci. Transl. Med. 4, 140 ra88.

Kim JH, Alfieri A, Kim SH, et al. , 1984. Radiosensitization of a meth-a fibro-sarcoma in mice by lonidamine. Oncology.

Kim JH, Alfieri AA, Kim SH, Young CW, 1986. Potentation of radiation effects on 2 murine tumors by londimaine. Cancer Res.

Knowles H, Harris A, 2001. Hypoxia and oxidative stress in breast cancer Hypoxia and tumourigenesis. Breast Cancer Res. 3 (5).

Kolesnick R, Fuks Z, 2003. Radiation and ceramide-induced apoptosis. Oncogene 22, 5897–5906. [PubMed: 12947396]

Lacerda Q, Tantawi M, Leeper DB, Wheatley MA, Eisenbrey JR, 2021. Emerging applications of ultrasound-contrast agents in radiation therapy. Ultrasound Med. Biol. 47 (6), 1465–1474 [PubMed: 33653626]

Lechner M, Liu J, Masterson L, Fenton TR, 2022. HPV-associated oropharyngeal cancer: epidemiology, molecular biology and clinical management. Nat. Rev. Clin. Oncol. 1, 1–22.

Lehnert S, 2007. Biomolecular Action Of Ionizing Radiation. CRC Press, Boca Raton.

Liang KY, Zeger SL, 1986. Longitudinal data analysis using generalized linear models. Biometrika 73 (1), 13–22.

Magno L, Terraneo F, Bertoni F, Tordiglione M, Bardelli D, Rosignoli MT, Ciottoli GB, 1994. Double-blind randomized study of lonidamine and radiotherapy in head and neck cancer. Int. J. Radiat. Oncol. Biol. Phys. 29 (1), 45–55. [PubMed: 8175445]

Marur S, Forastiere A, 2016. Head and neck squamous cell carcinoma: update on epidemiology, diagnosis, and treatment. Mayo Clin. Proc. 91 (3), 386–396. [PubMed: 26944243]

McEwan C, Owen J, Stride E, Fowley C, Nesbitt H, Cochrane D, Coussios CC, Borden M, Nomikou N, McHale AP, Callan JF, 2015. Oxygen carrying microbubbles for enhanced sonodynamic therapy of hypoxic tumours. J. Control Release 203, 51–56. [PubMed: 25660073]

Milane L, Duan ZF, Amiji M, 2011. Pharmacokinetics and biodistribution of lonidamine/paclitaxel loaded, EGFR-targeted nanoparticles in an orthotopic animal model of multi-drug resistant breast cancer. Nanomedicine 7 (4), 435–444. [PubMed: 21220050]

Moulder J, Rockwell S, 1984. Hypoxic fractions of solid tumors: Experimental techniques, methods of analysis, and a survey of existing data. Int. J. Radiat. Oncol. Biol. Phys. 10 (5), 695–712. [PubMed: 6735758]

Mullick Chowdhury S, Lee T, Willmann JK, 2017. Ultrasound-guided drug delivery in cancer. Ultrasonography 36 (3), 171–184. [PubMed: 28607323]

Nancolas B, Guo L, Zhou R, et al. , 2016. The anti-tumour agent lonidamine is a potent inhibitor of the mitochondrial pyruvate carrier and plasma membrane monocarboxylate transporters. Biochem. J. 473 (7), 929–936. [PubMed: 26831515]

Nath K, Guo L, Nancolas B, et al. , 2016. Mechanisms of antineoplastic activity of lonidamine. Biochim. Biophys. Act.

Nordsmark M, Bentzen S, Rudat V, et al. , 2005. Prognostic value of tumor oxygenation in 397 head and neck tumors after primary radiation therapy. an international multi-center study. Radiother. Oncol. 77 (1), 18–24. [PubMed: 16098619]

Oeffinger B, Vaidya P, Ayaz I, Shraim R, Eisenbrey J, Wheatley M, 2019. Preserving the integrity of surfactant-stabilized microbubble membranes for localized oxygen delivery. Langmuir 35 (31), 10068–10078. [PubMed: 30827115]

Patel R, Lacerda Q, Oeffinger BE, Eisenbrey JR, Rochani AK, Kaushal G, Wessner CE, Wheatley MA, 2022. Development of a dual drug-loaded, surfactant-stabilized contrast agent containing oxygen. Polymers 14 (8), 1568. [PubMed: 35458319]

Price G, Page R, Riviere J, et al. , 1996. Pharmacokinetics and toxicity of oral and intravenous lonidamine in dogs. Cancer Chemother. Pharmacol. 38, 129–135. [PubMed: 8616902]

Reusser TD, Song KH, Ramirez D, Benninger RK, Papadopoulou V, Borden MA, 2020. Phospholipid oxygen microbubbles for image-guided therapy. Nanotheranostics 4, 83–90. [PubMed: 32190535]

Rochani AK, Wheatley M, Oeffinger BE, Eisenbrey JR, Kaushal G, 2020. LC-MS based stability-indicating method for studying the degradation of lonidamine under physical and chemical stress conditions. Res. Pharm. Sci.

Rockwell S, Dobrucki I, Kim E, Marrison S, Vu V, 2009. Hypoxia and radiation therapy: past history, ongoing research, and future promise. Curr. Mol. Med. 9 (4), 442–458. [PubMed: 19519402]

Siegel R, Miller K, Jemal A, 2019. Cancer statistics, 2019. CA Cancer J. Clin. 69 (1), 7–34. [PubMed: 30620402]

Srinivas US, Tan BWQ, Vellayappan BA, Jeyasekharan AD, 2019. ROS and the DNA damage response in cancer. Redox Biol. 25, 101084. [PubMed: 30612957]

Vaidya P, Oeffinger BE, Patel R, Lacerda Q, Powell J, Eisenbrey JR, Wheatley MA, 2021. Shaping the synthesis of surfactant-stabilized oxygen microbubbles to accommodate encapsulated drug. Colloids Surf., B 208.

Vigneswaran N, Williams M, 2014. Epidemiologic trends in head and neck cancer and aids in diagnosis. Oral Maxillofac. Surg. Cli.n North Am. 26 (2), 123–141.

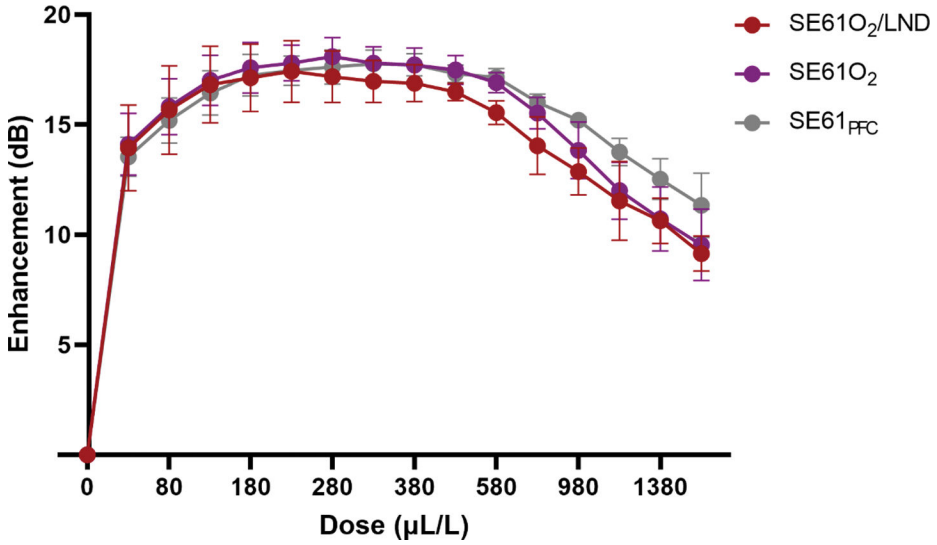

Fig. 1.
Effect of filling gas and drug content on dose response curves.

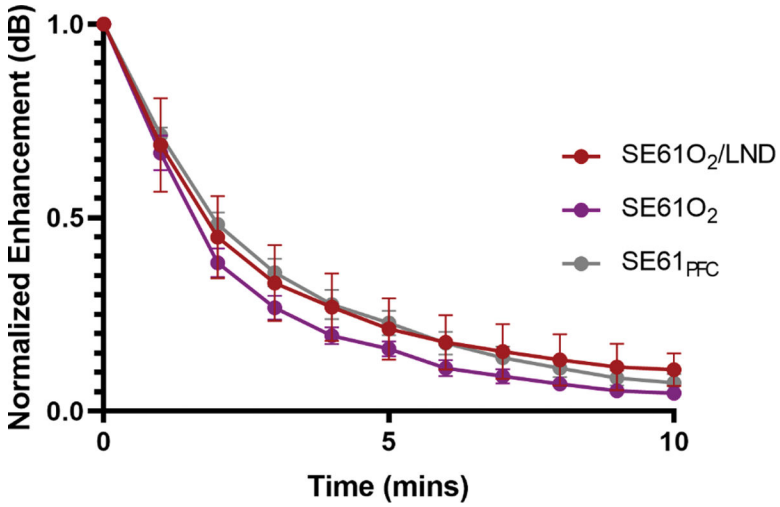

Fig. 2.
Effect of filling gas and drug content on *in vitro* stability.

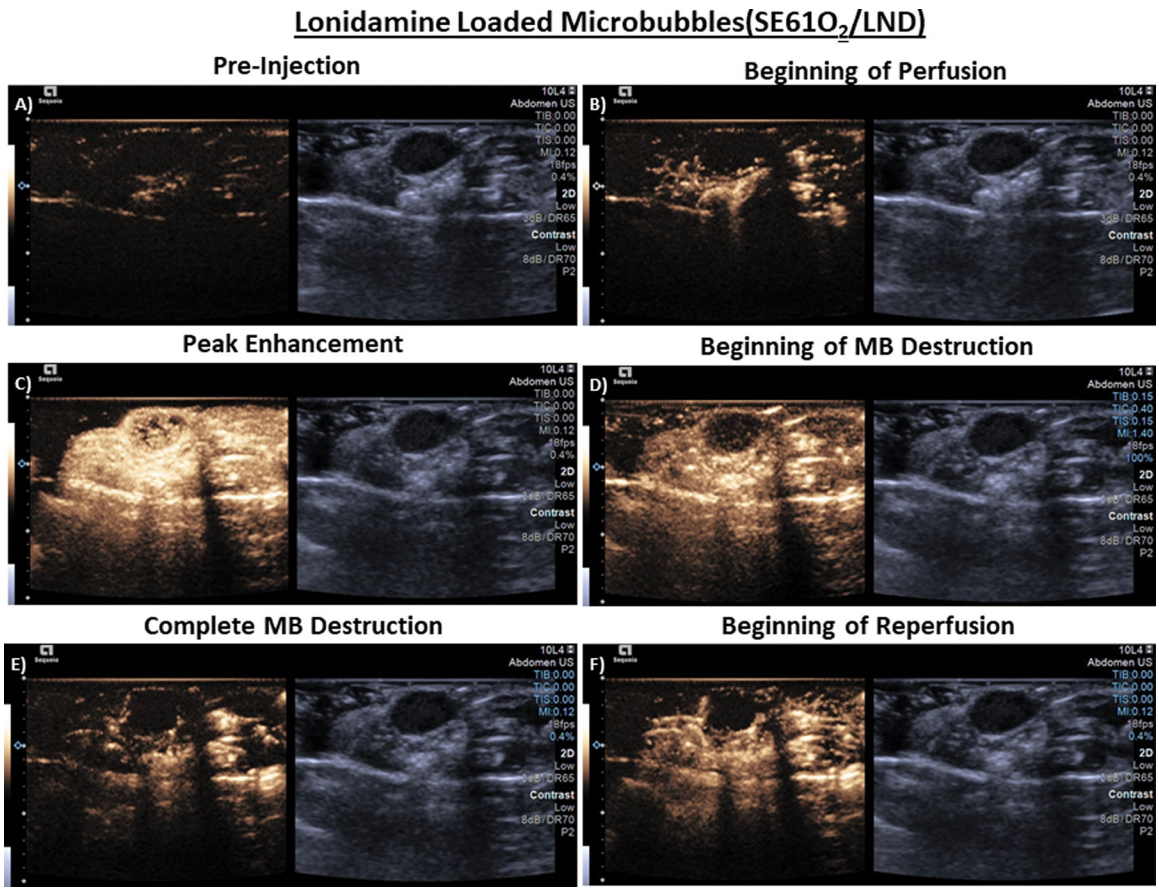

Fig. 3.

Ultrasound images in athymic nude mice taken in dual B-mode/cadence pulse sequencing mode, imaging subcutaneous CAL27 human squamous cell carcinoma. A) Pre tail-vein injection of microbubbles (MB) (tumor outlined in red), B) Start of MB perfusion, C) Peak enhancement post injection D) Start of MB destruction E) Complete MB destruction F) Start of reperfusion (image depth corresponds to 0.2 cm increments). (For interpretation of the references to colour in this figure legend, the reader is referred to the web version of this article.)

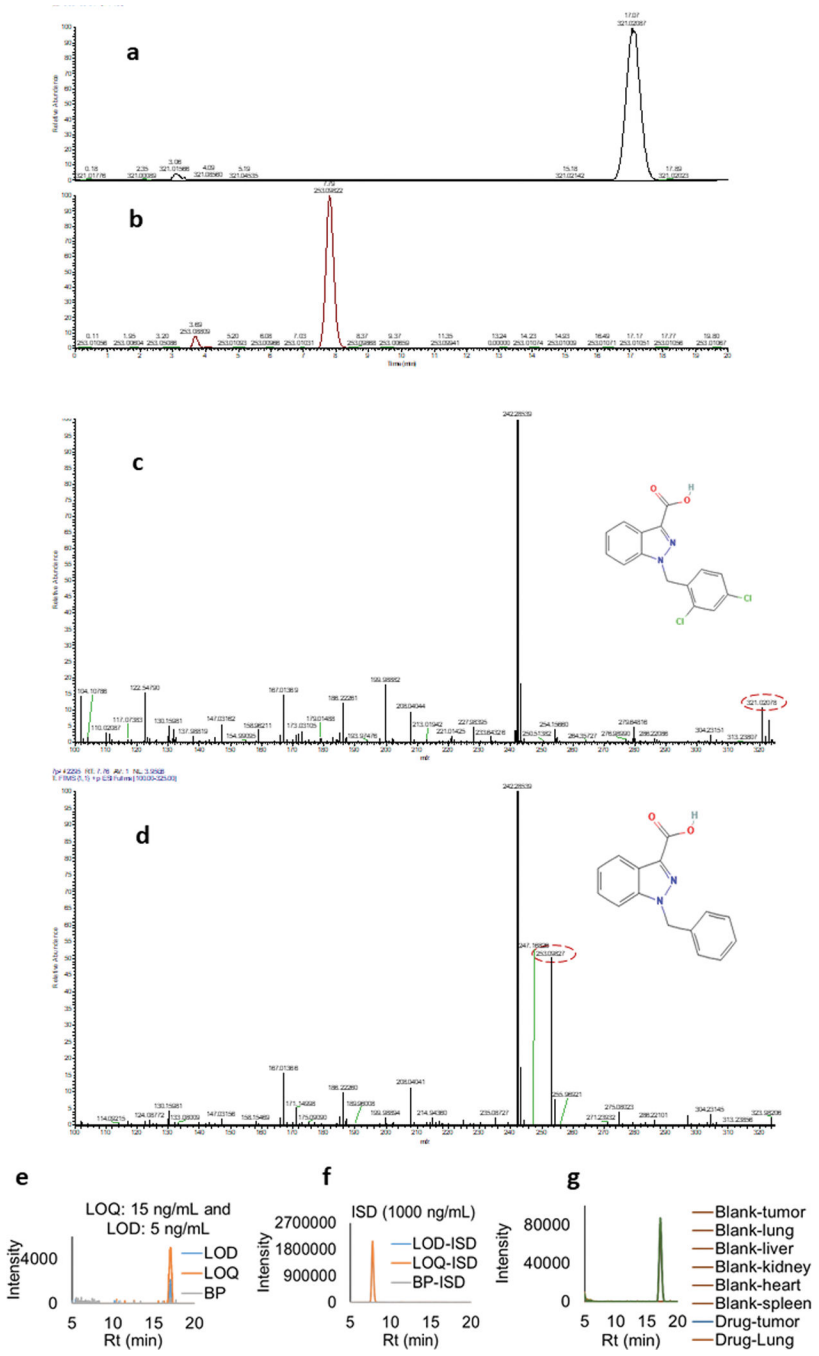

Fig. 4.

(a and b) LCMS spectra for LND (Rt:17.07 min) and ISD (Rt: 7.79 min). (c and d) Corresponding mass spectra for LND ($(M + H)^+$ 321.02 *m*/*z*) and 1-benzyl imidazolyl-3-carboxylic acid ($(M + H)^+$ 253.09 (*m*/*z*)). (e and f) LOD and LOQ extracted ion chromatogram (XIC) spectra overlay for LND. Corresponding ISD spectra overlay was also provided. Data clearly shows no interference from the matrix background. (g) XIC overlay for the blank tissue and 500 ng/mL drug spiked tissue extracted in ACN show consistent recovery for all the samples.

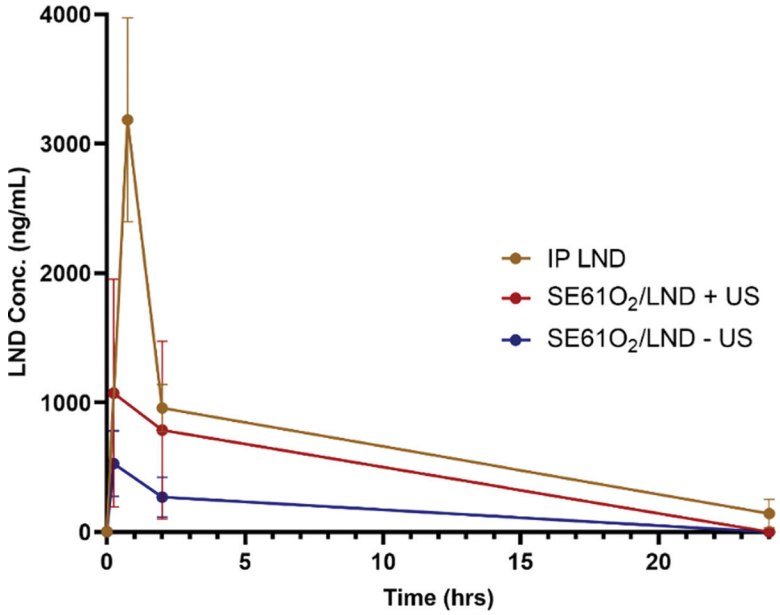

Fig. 5.

Effect of treatment on LND concentration in plasma with and without ultrasound triggering (+and − US).

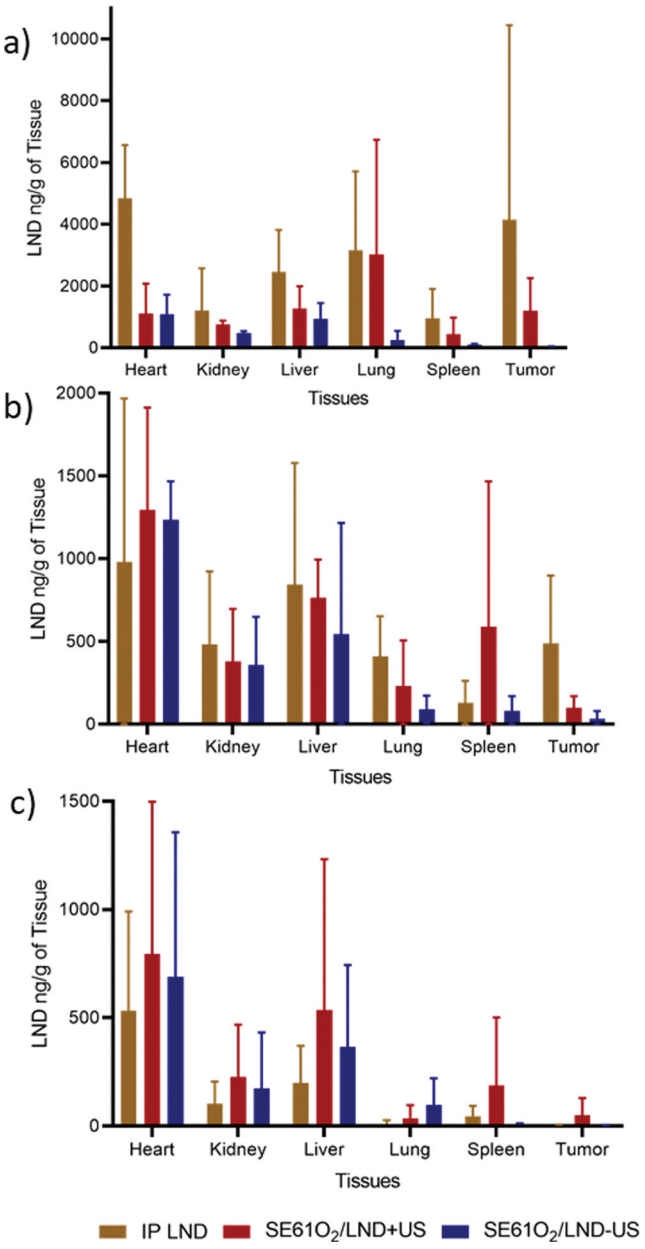

Fig. 6.

Effect of treatment on LND concentration in ng/g of tissue at time a) 2 hrs. b) 24 hrs. and c) 72 hrs with and without ultrasound triggering (+and − US).

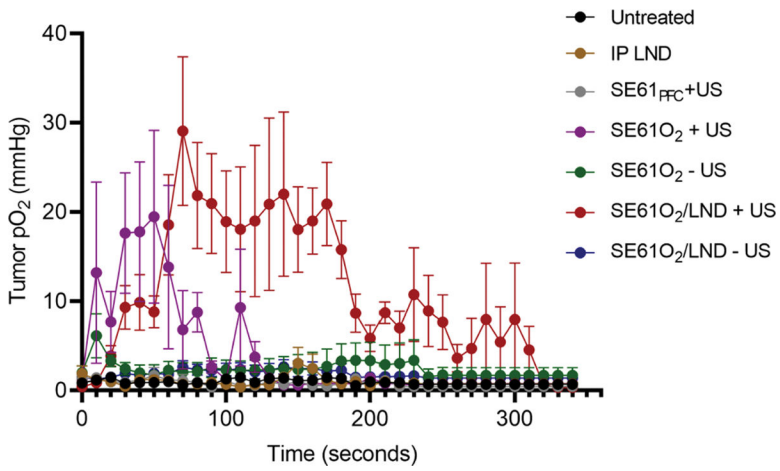

Fig. 7.

OxyLite measurement data showing sustained elevation of tumoral oxygen partial pressure (pO_2) when $SE61O_2$ and $SE61O_2$/LND are insonated with ultrasound (+US) shown in purple and red, respectively. (For interpretation of the references to colour in this figure legend, the reader is referred to the web version of this article.)

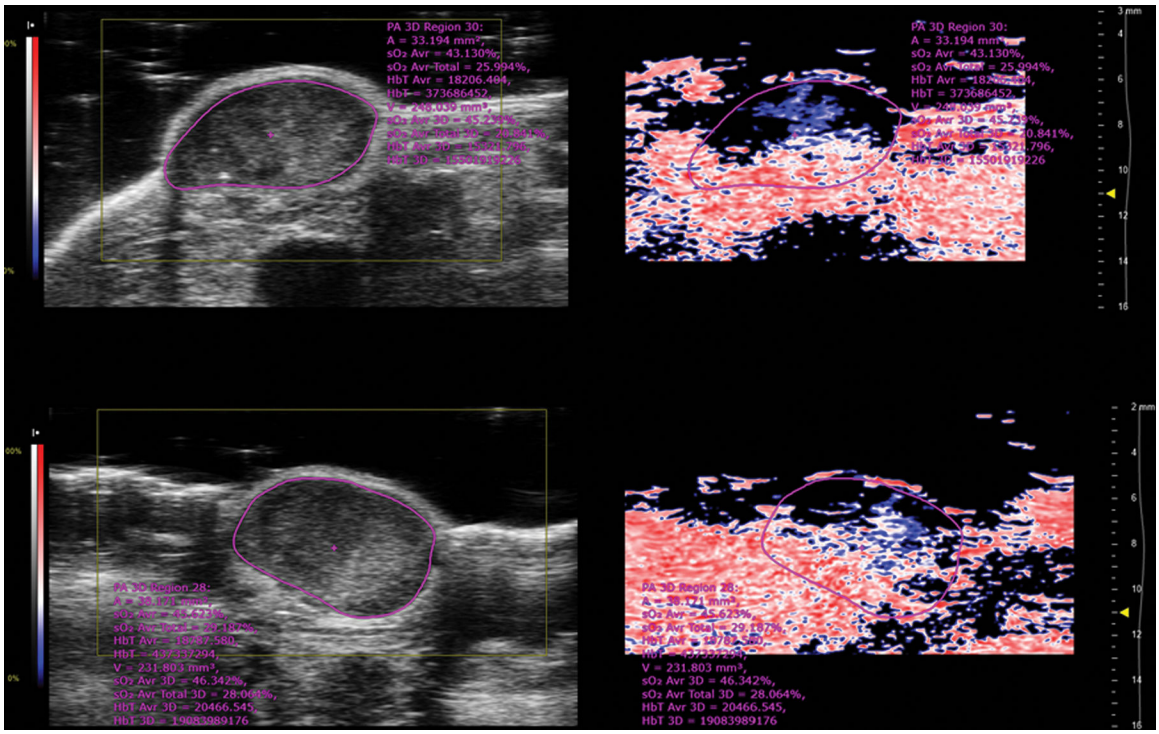

Fig. 8.

Example of photoacoustic images showing B-mode ultrasound on the left frame of the image (in greyscale) with photoacoustic signal on the right side of the image (low oxygen saturation shown in blue; higher oxygen saturation shown in red). The top image is prior to injection of microbubble triggering. Bottom image is following SE61O_2 injection and triggering. No changes of hemoglobin oxygenation were observed (image depth corresponds to 0.5 mm increments). (For interpretation of the references to colour in this figure legend, the reader is referred to the web version of this article.)

Table 1

Treatment groups.

Group	Treatment	Ultrasound	n
1	none	no	8
2	IP LND	no	8
3	$SE61_{PFC}$	yes	8
4	$SE61O_2$	yes	8
5	$SE61O_2$	no	8
6	$SE61O_2$/LND	yes	8
7	$SE61O_2$/LND	no	8

Table 2

Tumor tissue-specific linear model results

PARAMETER	TREATMENT	ESTIMATE	95 % CI	p
Intercept		7.2304	(6.0862, 8.3745)	<0.001
	IP LND	−0.1011	(−1.4433, 1.2412)	0.883
	$SE61O_2$/LND − US	−2.766	(−3.9817, −1.5503)	<0.001
	$SE61O_2$/LND + US	Reference		
Time, log (hours)		−0.8393	(−1.2333, −0.4454)	<0.001